



Forecasting failure locations in 2-dimensional disordered lattices

Estelle Berthier^{a,1}, Mason A. Porter^b, and Karen E. Daniels^a

^aDepartment of Physics, North Carolina State University, Raleigh, NC 27695; and ^bDepartment of Mathematics, University of California, Los Angeles, CA 90095

Edited by Stefano Zapperi, University of Milan, Milan, Italy, and accepted by Editorial Board Member Herbert Levine June 21, 2019 (received for review January 8, 2019)

Forecasting fracture locations in a progressively failing disordered structure is of paramount importance when considering structural materials. We explore this issue for gradual deterioration via beam breakage of 2-dimensional (2D) disordered lattices, which we represent as networks, for various values of mean degree. We study experimental samples with geometric structures that we construct based on observed contact networks in 2D granular media. We calculate geodesic edge betweenness centrality, which helps quantify which edges are on many shortest paths in a network, to forecast the failure locations. We demonstrate for the tested samples that, for a variety of failure behaviors, failures occur predominantly at locations that have larger geodesic edge betweenness values than the mean one in the structure. Because only a small fraction of edges have values above the mean, this is a relevant diagnostic to assess failure locations. Our results demonstrate that one can consider only specific parts of a system as likely failure locations and that, with reasonable success, one can assess possible failure locations of a structure without needing to study its detailed energetic states.

failure | lattices | networks | centrality

Cellular foams (1), semiflexible fiber and polymer networks (2), and many recently developed mechanical metamaterials (3–5) all belong, in idealized form, to a general class of disordered lattices. Such lattices can range in size from microscopic scaffolds for biological tissue growth (6) to modern architectural structures (7). In each case, one can further idealize the material or structure as a mathematical network of connections between slender beams that intersect at various points within the material. From an engineering perspective, such materials are promising because of their light weights and their tunable, designable properties: a Poisson ratio from the auxetic (4, 8, 9) to the incompressible limits (4), a targeted local response to a remote perturbation (5), or the ability to change shape (3). A disadvantage of these materials is that those that are constructed from stiff materials can degrade progressively through successive abrupt failures of the beams during loading (8, 10, 11). To design optimized structures and safely use them for structural applications, it is necessary to assess the most likely locations of fracture. Such predictive understanding would further enable the design of a material to fail in a prescribed way.

Fracture experiments have been conducted previously on printed, disordered auxetic materials (8) and 2-dimensional (2D) laser-cut, disordered honeycomb lattices (10). In these studies, very different fracture behaviors (ductile vs. brittle) have been obtained by changing the loading direction (8) or tuning the rigidity (10). In the latter study, a clear change arose in the spatial organization of fractures: they can either be dispersed throughout a system or be localized in the form of a narrow crack. Therefore, although some tunable parameters for controlling failure behavior have been identified, what determines these particular failure locations remains an open question. According to the theory of Griffith (12), damage in brittle materials focuses at the tip of a crack. However, factors such as material disorder (13–17), material rigidity (10), and

the connectivity (specifically, mean degree) of networks (10, 18) can affect the spatial organization of damage. As one tunes each of these factors, one can make failures spread throughout a system (diffuse damage) rather than form a narrow crack (localized damage).

Zhang and Mao (11) showed recently that failures can also be delocalized in topological Maxwell lattices (in which freely rotating joints that are linked by rigid struts are on the verge of mechanical instability) (19). They performed numerical experiments on the tensile fracture of deformed square and kagome lattices, demonstrating that stress and fracture concentrate on self-stress domain walls, even in the presence of damage that is introduced elsewhere in the system. In another recent paper, Tordesillas et al. (20) studied damage locations in discrete element simulations of concrete samples under uniaxial tension. From a network-flow analysis of the contact-network topology and contact capacities of a specimen, the authors determined the location of the principal interacting macrocracks. In their samples, they observed that secondary macrocracks develop in the prefailure regime after damage occurs elsewhere, but before the formation of a dominant macrocrack that sets the ultimate failure pattern of a sample.

In this paper, we investigate where damage occurs in disordered lattices that consist of identical-width beams, with a network topology specified by contacts that are measured from a real quasi-2D granular packing (Fig. 1). We identify a common property, a large value of geodesic edge betweenness centrality (GEB) (25), that is shared by the failure locations of progressive damage events of our tested samples. Even without modeling

Significance

Disordered lattices are used widely for mechanical applications because they are lightweight and robust. Due to their heterogeneous structure, it is a complicated task to understand and forecast their progressive degradation. To safely use these materials and design structures with optimized mechanical properties, it is crucial to understand where failures occur. We show that a simple test that consists of comparing the importance of a beam with respect to the other beams in a lattice permits a successful forecast of the locations of failures. It allows one to consider only a small fraction of the beams as likely failure locations. Our approach also provides a roadmap for studies of failures in other spatial networks.

Author contributions: E.B., M.A.P., and K.E.D. designed research, performed research, analyzed data, and wrote the paper, with E.B. as the lead researcher.

The authors declare no conflict of interest.

This article is a PNAS Direct Submission. S.Z. is a guest editor invited by the Editorial Board.

Published under the PNAS license.

See Commentary on page 16666.

¹To whom correspondence may be addressed. Email: ehberthi@ncsu.edu.

This article contains supporting information online at www.pnas.org/lookup/suppl/doi:10.1073/pnas.1900272116/-DCSupplemental.

Published online August 2, 2019.

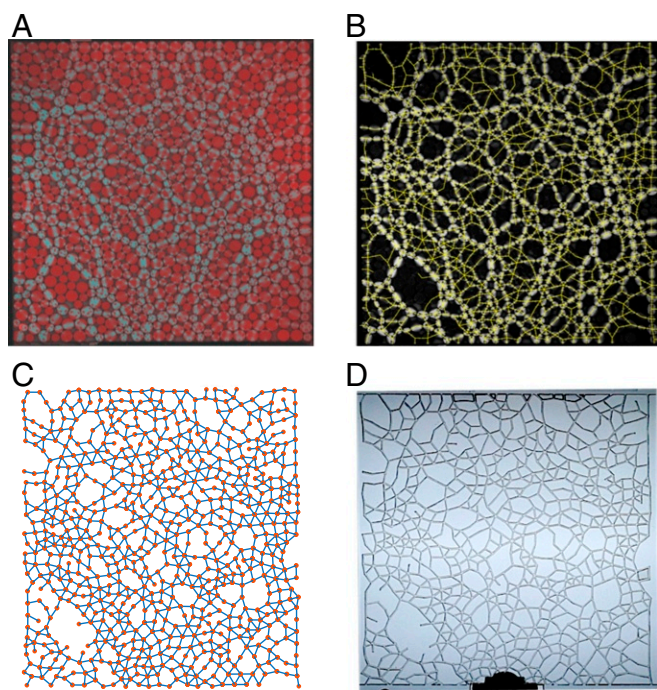


Fig. 1. (A) Force chains (cyan) recorded in a 2D assembly of frictional photoelastic disks (red), which we image via a circular polariscope (21). Brighter particles carry stronger forces. (B) Contact network (yellow), which was extracted using an open-source photoelastic solver (21–23), overlaid on the reconstructed “pseudo-image” (21). (C) Network representation in which each particle center is a node (orange dots) and each load-bearing contact is an edge (blue lines) (24). (D) Corresponding physical sample that we laser cut from an acrylic sheet, with the edges represented by beams that intersect at cross-links (which correspond to the nodes in the network).

the physical interactions between nodes, this property provides a diagnostic for identifying likely failure locations. Such an indicator would permit assessing these locations in a structure without studying its detailed energetic or stress states. Ultimately, the choice of a granular-inspired geometry for a disordered lattice will provide a route toward generalizing these studies across inherently different systems, which are linked by their network topology.

For each network, we laser cut an acrylic sheet using a contact network that matches the one observed in a packing, and we then test its behavior under compressive or tensile loading. Because the set of contacts in a packing forms a network that is embedded in a plane, our lattice does as well. Such a lattice network consists of edges (representing the beams of the lattice) that intersect at nodes, which occur at the cross-links of the lattice. Conceptually similar structures occur in streets and intersections in the study of road networks (26, 27), connections between internet routers, plant veins (28), fungi (29), and many other spatial systems (30, 31).

Network analysis provides useful approaches—including measures, algorithms, and theory—for characterizing complex spatial systems at multiple scales, ranging from local features to mesoscale and macroscale ones, and examining how they evolve (24, 32). As discussed by Smart and Ottino (33), it is appealing to investigate what insights network analysis and associated topics (e.g., graph theory and algebraic topology) can yield on physical systems, especially in comparison with traditional approaches. For example, this perspective was adopted by Tordesillas et al. (20) to study quasibrittle failure using network-flow analysis. Such approaches have also been useful for the study of mesoscale structures, such as dense communities of nodes, in granular sys-

tems (34). Therefore, network analysis seems to be a promising route to identify common analytical tools that are capable of relating failure behaviors across a variety of disordered systems.

One important approach in network analysis is the calculation of “centrality” measures to ascertain the most important nodes, edges, and other subgraphs in a network (32, 35). One particularly popular type of centrality, known as betweenness centrality, measures whether one or more parts of a network lie on many short paths; it has been used to characterize the importance of nodes (36), edges (25), and other subgraphs. The most common type of betweenness centrality uses geodesic (i.e., strictly shortest) paths.

Recently, in a study of granular materials, Kollmer and Daniels (37) showed that there is a positive correlation between the geodesic betweenness centrality value of a node and the pressure on the corresponding particle. Previously, Smart et al. (38) reported that edges with large geodesic betweenness centrality exert a strong influence on heat transport in granular media. Inspired by these investigations, we selected from among the variety of network measures (31, 32) and focus on calculating GEBC. We show its definition in Eq. 5 (see *Materials and Methods*).

As was reported in Berthier et al. (23), one can control the compressive and tensile failure behaviors of a disordered lattice by tuning the mean degree of its associated network. This control parameter provides a way to create systems with a variety of failure behaviors, ranging from ductile-like to brittle-like failure. In this paper, we show for samples across the spectrum from brittle-like to ductile-like failure (see *Mechanical Testing Protocol*) that individual beam failures occur predominantly on edges with GEBC values that are above the mean of the network. From this result, we conclude that GEBC is a useful diagnostic for forecasting possible failure locations in our contact networks. We demonstrate the ability of a GEBC-based test, which consists of comparing the GEBC value of an edge with a threshold value, to discriminate between beams that fail and those that remain intact. This finding, together with the work of ref. 38, suggests that betweenness centrality is a useful measure for capturing essential physical properties in disordered systems. Our study also confirms that tools from network analysis give a promising paradigm for the study of fracture.

The effectiveness of GEBC, which depends on network topology rather than on specifying mechanical interactions, is unexpected. This motivates a deeper analysis to determine which behaviors do not depend primarily on the detailed physical properties of a system, but instead depend on its geometry (and associated network topology). Our use of unweighted networks focuses our investigation on network topology, and we compare results for both a measure (specifically, GEBC) that ignores the physics and a well-known scalar electrical analogy of elasticity known as a random fuse network (RFN) model (17, 39). The RFN model identifies the most stressed beams as the edges with the largest currents, as determined by solving Kirchhoff’s laws, for a given voltage drop across the boundaries. We show that the RFN model, even with its incorporation of physical considerations, does not markedly improve performance over GEBC. This indicates that one can capture essential features of lattice failure behavior by geometric (rather than physical) considerations.

Results

Spatial Heterogeneity and Changes with Applied Strain of GEBC.

We examine the ability of GEBC \tilde{E} (Eq. 5) to forecast the specific locations at which our samples fail. For each initial (and subsequently altered) network, we find that geodesic edge betweenness takes a broad range of values across the network. In Fig. 24, we show the probability density function (PDF) of the initial geodesic edge betweenness \tilde{E}_0 for each initial network at each value of the mean degree \bar{z}_0 . To facilitate notation,

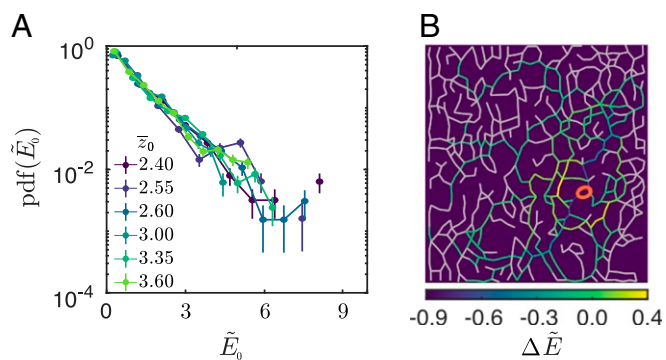


Fig. 2. Characterization of geodesic edge betweenness (re-)distribution. (A) PDF of the initial GEBC \tilde{E}_0 for the different initial networks. We show the PDFs for several values of mean degree. (B) Changes in GEBCs \tilde{E} after a failure event that occurs at the red ellipse at a compressive strain of $\varepsilon \approx 1.98\%$ on a network with mean degree $\bar{z}_0 = 2.40$. The values of the lavender edges change by less than 10^{-2} .

we use the subscript 0 to designate our initial networks and the quantities that we measure and compute with them. In all cases, the distribution of values is approximately exponential, and it is largely independent of \bar{z}_0 . Because each failure event (with associated edge removals) results in a new set of shortest paths, we obtain a new distribution of GEBC values for each altered network. Just as stress redistributes after damage (40–43), GEBC (due to its nonlocal nature) also redistributes in a system. In Fig. 2B, we show a characteristic example of redistribution after a failure event. The redistributions are system-wide: some edges are “reloaded,” becoming more important with respect to the others (i.e., $\tilde{E}_{s+1} > \tilde{E}_s$ when going from strain step s to strain step $s + 1$), others are “unloaded” (i.e., $\tilde{E}_{s+1} < \tilde{E}_s$), and some edges (in lavender in Fig. 2B) have the same (or almost the same) value. By contrast, removal of unimportant edges (i.e., those with small values of GEBC) results in small (in amplitude) changes.

Damage occurs progressively through a sequence of tensile or compressive loading. In Fig. 3, we show examples of damage progression for 3 values (1 per row) of \bar{z}_0 . Within each row, a sample progresses from its initial intact network G_0 (an unweighted and undirected graph) through an altered network at which about 50% of its beams have failed, and then to the network immediately before the final failure. For each row of Fig. 3, in the network immediately after the last image that we show, there is no longer a set of beams that connects the top and bottom boundaries of the sample. We color each edge in each network according to the value of \tilde{E}_s at that strain step.

Geodesic edge betweenness is spatially heterogeneous across a network, and we observe that large values (bright colors) can occur throughout a network. These locations shift both in space and in time due to the disordered structure (which arises from geometry) of our lattices. By contrast, for a regular lattice, the importance of edges decreases with their distance from the geometric center of a system (31). The introduction of disorder—such as by rewiring, addition, or removal of edges—results in more complicated distributions and can lead to geographically central edges with smaller importance than elements that are farther from the geometric center (44). Importantly, although the topologies of the networks underlying our lattices are inherited from uniaxially compressed granular packings, we do not observe a preferred orientation for edges with GEBC values that are above the mean. Granular packings encode their preparation history in the form of anisotropic stresses (45, 46), but this anisotropy is not readily identifiable from the contact network (which is unweighted).

The GEBC values at a given strain step illustrate the broad distribution of values, as we observed in the exponential PDF of \tilde{E}_0 (Fig. 2). Even in these small systems, some edges have values up to 20 times the mean of the system; these are ones that are particularly important for connecting different parts of a network. Many other edges occur only infrequently as shortest-path connectors. The variations in spatial distribution along the rows of Fig. 3 highlight the importance of the removed edges, as we emphasized in Fig. 2B. Importantly, although \tilde{E} tends to decrease with distance from the geometric center, this need not be true for specific samples. For the near-final networks (Fig. 3, *Right*) at $\bar{z}_0 = 2.40$ and $\bar{z}_0 = 3.00$, the maximum of \tilde{E} is located near the left boundary of the sample, rather than near the middle. In both cases, the largest values of \tilde{E} occur on edges that connect the top and bottom parts of the network, and these are also the next beams that will break (and lead to the final cascade of failures).

GEBCs of Failed Edges. Such observations suggest that there is a correlation between large values of \tilde{E} and future failure locations. To assess the generality of this finding, for each breaking beam, we calculate the GEBC \tilde{E}_f during step $s - 1$ immediately before its failure at step s . For all of our samples and for all small failure events (which we take to mean that no more than 3 beams are involved), we enumerate the immediately preceding values of \tilde{E} for the failed edges. In Fig. 4A, we show the cumulative distribution function (CDF) of this set of values, together with the corresponding PDF in Fig. 4A, *Inset*. We fit the PDF with an exponential with mean $\tilde{E}_f^* \approx 10.3$ (with $R^2 \approx 0.96$). There is a corresponding gradual increase for $\tilde{E}_f \gtrsim 10$ of the CDF, suggesting that few failing edges have a value that is significantly larger than the mean. We observe such large values of \tilde{E} only when the samples are near full failure; at this point, only a few paths are available to connect the top and bottom boundaries of the network. One can see this situation in Fig. 3, *Right*. Focusing on $\tilde{E}_f = 1$, we see that about 76% of the breakages occur on edges with values of \tilde{E}_f that are above the mean. Because only a small subset of the network's edges have $\tilde{E} > 1$ (see the distribution in Fig. 2A), even the value of \tilde{E} alone is a valuable diagnostic for forecasting failure locations.

We can refine this diagnostic by directly considering the population of edges that exceed a threshold value \tilde{E}_{th} . We illustrate this population by plotting the complementary cumulative distribution function (CCDF) on the left vertical axis in Fig. 4B. Because the proportion of edges that satisfy $\tilde{E} > \tilde{E}_{th}$ evolves after each edge removal and differs across initial networks, we choose each point of the curve to be the maximum value that we encounter among all networks. The success rate of this diagnostic is the fraction of failed beams that satisfy $\tilde{E} > \tilde{E}_{th}$, and the failure rate is the fraction for which $\tilde{E} \leq \tilde{E}_{th}$. We show the latter as orange diamonds on the right vertical axis of Fig. 4B for all small failure events among all tested samples, regardless of the tensile or compressive nature of the applied loading. In Fig. 4C, we focus on the point at which the CCDF and the failure-rate curves cross; this intersection occurs at $\tilde{E}_{th} \approx 1.1$, corresponding to a value on the CCDF curve (i.e., the fraction of edges for which $\tilde{E} \gtrsim 1.1$) of about 0.34 and a failure rate of about 0.26. This intersection point indicates that considering all edges with above-mean GEBC values provides a reasonable population of edges to consider, but one can choose other values in a tradeoff between forecast failure rate and the fraction of examined edges.

The above general results exhibit sample-to-sample variation. To highlight this, we include an envelope of the failure rate in

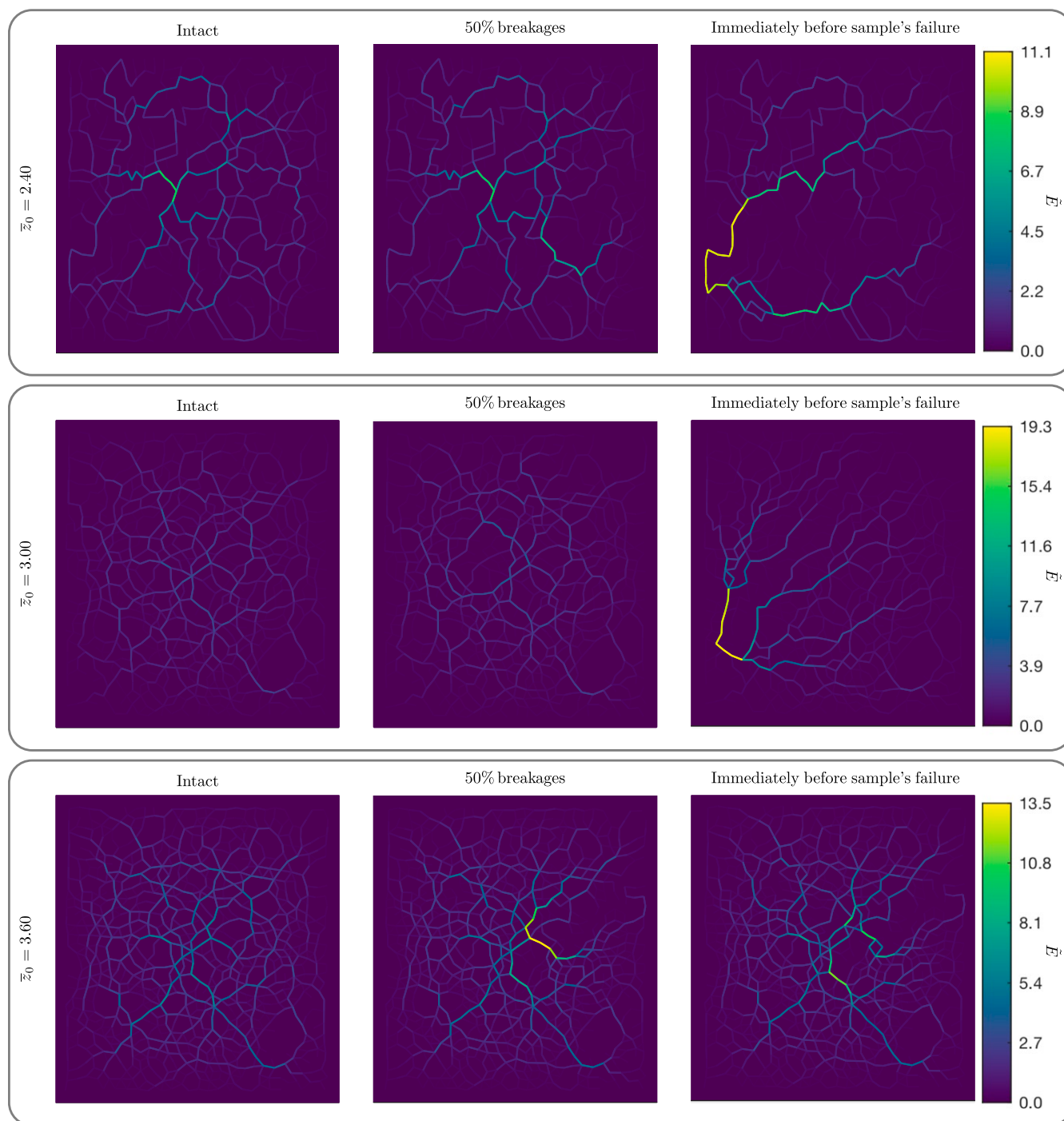


Fig. 3. Example images of the spatial distribution of normalized GEBCs \tilde{E} (given by the color bar), which we plot at a particular applied strain ε (in *Mechanical Testing Protocol*, we discuss the strain steps) for samples that are subject to compression. The rows show samples with (Top) $\bar{z}_0 = 2.40$, (Middle) $\bar{z}_0 = 3.00$, and (Bottom) $\bar{z}_0 = 3.60$. Within each row, we show the progression (of strain steps) in ε from (Left) initial intact networks G_0 with adjacency matrix A_0 to (Center) the step at which 50% of breakages have occurred (with $\varepsilon \approx 3.39$, $\varepsilon \approx 1.68$, and $\varepsilon \approx 1.90\%$ from Top to Bottom), and finally to (Right) the strain step immediately before a system-spanning failure (with $\varepsilon \approx 9.56$, $\varepsilon \approx 3.66$, and $\varepsilon \approx 1.95\%$ from Top to Bottom).

Fig. 4C. To obtain this envelope, we determine a failure-rate curve for each of the 14 samples (see *Materials and Methods*). We obtain each curve by examining the failure events that occur on each initial intact network. For each threshold value, we track the best (lower point) and worst (upper point) failure-rate value among the 14 curves. The envelope is the set of points between these lower and upper bounds for each threshold value. Although the scatter is nonnegligible, for a threshold

of $\tilde{E}_{th} = 1$, we still obtain success rates above 65% for all samples.

Test Sensitivity and Specificity. Performing sensitivity and specificity analyses (47) allows a more detailed determination of the suitability of using $\tilde{E} > \tilde{E}_{th}$ to identify beams that are likely to fail. We define the outcome of this test as true positive (TP), false positive (FP), true negative (TN), or false negative (FN)

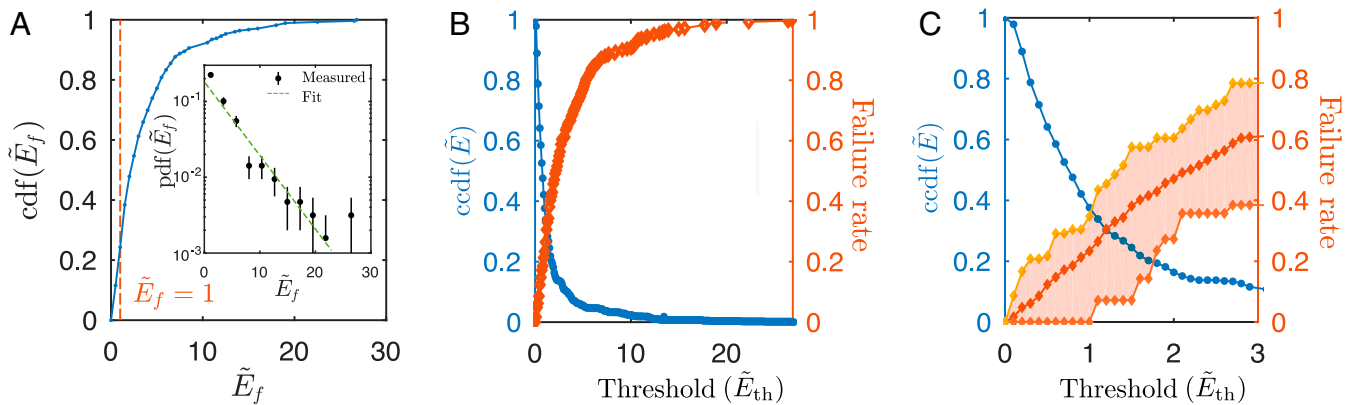


Fig. 4. (A) CDF of GEBC of failed edges of all experiments. We show the PDF in the *Inset*. (B) Fraction of edges in the network for which $\tilde{E} > \tilde{E}_{th}$ (blue dots, left axis) and fraction of failed beams for which $\tilde{E} \leq \tilde{E}_{th}$ (orange diamonds, right axis). (C) Magnification of the cross-over point between the CCDF and the failure rate (and the envelope of the results of individual samples).

according to the state of the beam (failing or remaining intact). We summarize these possible outcomes in Table 1.

“Sensitivity” is defined as the empirical probability of obtaining a positive test result for the population of failed beams (i.e., the proportion of TPs); therefore, $\text{sensitivity} = TP / (TP + FN)$. Similarly, “specificity” is the empirical probability of obtaining a negative test result for the population of intact beams (i.e., proportion of TNs); therefore, $\text{specificity} = TN / (TN + FP)$. These 2 measures quantify the success of our test for correctly identifying beams that will fail or remain intact.

We calculate sensitivity and specificity in considering all small failure events of all experiments as a function of the threshold \tilde{E}_{th} , and we show the results in Fig. 5A. As expected, sensitivity and specificity show opposite trends: as one lowers the threshold, the TP fraction (sensitivity) increases, but so does the FP fraction, such that the specificity (i.e., the TN fraction) decreases. As one increases the threshold, the opposite occurs: we obtain a smaller TP fraction (sensitivity decreases), and the FP fraction decreases (specificity increases). There is a cross-over between sensitivity and specificity at $\tilde{E}_{th} \approx 1.1$, which is close to the value 1 that we used above.

Computing a receiver operating characteristic (ROC) curve (48) provides additional insight into the choice of \tilde{E}_{th} . As we show in Fig. 5B, we measure sensitivity and specificity as a function of \tilde{E}_{th} . A test with perfect forecasting of failing vs. intact beams would go through the upper-left corner (in which sensitivity and specificity are both 1), and a test without any predictive power would follow the dashed diagonal line in Fig. 5B. (Anything below this line gives a result that is worse than random guessing and indicates that we should reverse our criterion, such that a positive test indicates “less than” rather than “greater than”.)

To obtain a global estimate of the accuracy of the test that goes beyond visual examination, we compute the area under the curve of the ROC curve. This ranges from 0.5 (no discrimination) to 1 (perfect accuracy). The value for the curve in Fig. 5B is 0.79, indicating a good capability of our test to discriminate between beams that will remain intact vs. those that will fail.

Discussion

Other Network Diagnostics and Approaches for Forecasting Failures. Motivated by the results in ref. 38 and the geometric origin of our samples, we have focused on using GEBC for forecasting failures in them. However, other network measures are also worth considering as possible diagnostics for forecasting failure locations. In particular, it is desirable to take advantage of the fact that the various flavors of betweenness are correlated with other quanti-

ties in certain types of networks. In some networks, for example, geodesic node betweenness can scale approximately with node degree (49). To give another example, Scellato et al. (50) studied the relation between GEBC and a quantity known as “information centrality” in networks based on the road systems of several cities. For the edge e_{ij} of a network, information centrality is

$$J_{ij} = \frac{F[G] - F[G']}{F[G]}, \quad [1]$$

where

$$F[G] = \frac{1}{N(N-1)} \sum_{i,j=1,\dots,N; i \neq j} \frac{d_{ij}^{Eucl}}{d_{ij}} \quad [2]$$

is the efficiency of an N -node graph G , the graph G' results from removing edge e_{ij} from G , the quantity d_{ij} is the distance between nodes i and j (e.g., from the smallest number of steps between i and j in an unweighted graph), and d_{ij}^{Eucl} is the Euclidean distance between those nodes.

We investigate the relation between GEBC and information centrality using a modified expression for efficiency, where we set $d_{ij}^{Eucl} = 1$ for all pairs (i, j) with $i \neq j$. To calculate information centrality, we compute efficiency using code from ref. 51. (We compute GEBC using the code “BETWEENNESS_WELM” and efficiency using “EFFICIENCY_WELM”.) Information centrality gives an indication of the perturbation of transmission across a network when one removes an edge. In other words, we ask the following question: how harmful is a beam failure for connections across a sample? When considering all edges of all of our networks (both initial and altered), we obtain a reasonably large correlation (with a Spearman rank correlation coefficient of 0.55 ± 0.014) of information centrality with GEBC. For failed edges, the Spearman correlation coefficient (0.77 ± 0.01) is even larger. Motivated by these calculations, we checked and confirmed that considering values above the mean for information centrality yields similar results as using GEBC as a test for potential failures. Therefore, information centrality is an alternative to GEBC to probe systems for likely failure locations. Measures based on shortest paths are not always highly correlated with each other (and the extent of

Table 1. Definition of the outcome of a test

Test: is $\tilde{E} > \tilde{E}_{th}$?	Beam fails	Beam does not fail
Positive	TP	FP
Negative	FN	TN

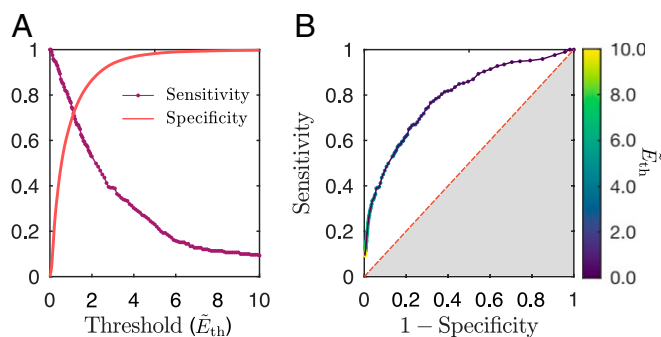


Fig. 5. Evaluation of our test's accuracy. (A) Sensitivity and specificity vs. the threshold \tilde{E}_{th} . (B) ROC curve summarizing the (sensitivity, $1 - \text{specificity}$) pairs that we obtain for different values of E_c . The dashed diagonal line indicates the behavior of a test that cannot discriminate between failing and intact beams.

such correlations also depends on network type) (27). Therefore, different measures related to betweenness can give complementary insights.

Comparison with Other Diagnostics. To disentangle the roles of physical and geometric effects, we evaluate the importance of introducing physical considerations by repeating our analysis using an RFN-based test (see *RFN Model*). In place of \tilde{E} , we determine the current \tilde{I} that flows through a network. As with GEBC, we determine the fraction of edges in a network with a current above a threshold current \tilde{I}_{th} and the fraction of failing beams for which $\tilde{I}_f \leq \tilde{I}_{th}$ (where \tilde{I}_f denotes the current of an edge during step $s - 1$ immediately before its failure at step s).

For threshold values in the range $[0, 2.5]$, we find that this test performs somewhat better than the test using GEBC (*SI Appendix, Fig. S1A*). However, in the range $[0, 1.4]$, the fraction of edges with a current above the threshold is slightly larger than the fraction of edges with a GEBC above the same threshold. Consequently, the tradeoff between the forecast failure rate and the fraction of possible edges differs between the 2 tests for the same threshold value. This tradeoff diminishes the advantage.

We also find that the current and GEBC values of the failed edges are positively correlated, with a Pearson correlation coefficient of $R \approx 0.81$ (*SI Appendix, Fig. S1B*). This suggests that failing beams, most of which have a larger stress than the mean value in a network (i.e., $\tilde{I}_f > 1$ for these edges), lie on many shortest paths, explaining the small improvement in forecast capability from using the RFN-based test. This finding is similar to the results of Kollmer and Daniels (37), who observed in 2D packings of frictional particles that ones with large node betweenness centralities are statistically likely to be highly stressed. Consequently, it is appropriate to examine betweenness centralities (of both nodes and edges) to capture important mechanical properties of physical systems.

Interestingly, as we show in *SI Appendix, Fig. S2*, the 2 tests do not systematically misdiagnose failure locations (i.e., yield FN outputs) for the same edges. Using the RFN-based test, we observe a correlation between beam angle and current flow (*SI Appendix, Fig. S3A*) and find a bias toward misdiagnosed edges that are roughly perpendicular to the loading direction (*SI Appendix, Fig. S3B*). It seems that failures occur at edges at all distances from the boundaries (*SI Appendix, Fig. S4A*). However, for some threshold values, most GEBC-misdiagnosed edges tend to occur near boundaries (*SI Appendix, Fig. S4B*), where large values of GEBC are less frequent.

The dependency of GEBC with distance from a sample's geometric center, even altered by the presence of disorder, is an important feature of networks that are embedded in a plane. To

examine whether we can circumvent this limitation of our GEBC test, we calculate GEBCs on a collection of modified networks. For a given network G and for each edge e_{ij} , we generate a duplicated network such that the edge e_{ij} is at the geometric center. To construct such a graph, we first duplicate the network with mirror symmetries with respect to each boundary. We then calculate the GEBC of e_{ij} by considering only a section of this duplicated network that is approximately centered at e_{ij} . We repeat this procedure for each edge of the network G to obtain centrality values for the network centered at that edge. Using this approach yields a cumulative distribution for \tilde{E}_f and a test ($\tilde{E}_f > \tilde{E}_{th}$) success rate similar to the original networks. Indeed, although boundary edges can have large \tilde{E} values, the distributions of \tilde{E} are more homogeneous than in the original networks, such that the test can misdiagnose edges in other locations. Consequently, the use of a duplicated network does not improve the forecasting ability of our approach. Preliminary calculations that account for the boundaries' loading (using master particles that are adjacent to corresponding loaded nodes) suggest that this simple physical consideration provides a way to improve our test's ability to forecast failure locations. Developing methods to appropriately consider the role of boundaries remains a central question for planar graphs—not only for granular materials, but also for other applications, such as determining high-traffic edges in road networks (27) and nutrient transportation networks (29)—and more generally in spatially-embedded networks.

In our comparison of GEBC-based and RFN-based tests, we observe a correlation between the physical and geometric properties of failing beams. Interestingly, a test that includes a minimal set of physical ingredients (i.e., the RFN-based test) performs only somewhat better than a test (the GEBC-based test) that is based on geometric considerations. Because these 2 tests have rather different limitations—with less successful forecasting of near-perpendicular edges vs. near-boundary edges—it is useful to use both as complementary approaches. Finally, it is worth noting that, although the RFN-based test is faster computationally than the GEBC-based one, neither approach requires significant computational resources for the system sizes that we consider in this study.

Conclusions

The idea, proposed in papers such as ref. 33 and reviewed in ref. 24 in the context of granular and particulate systems, to use network analysis to achieve insights on physical systems seems very promising for studies of fracture. In this paper, we explored the application of centrality measures (based on shortest paths) to forecast failure locations in physical samples. Many other tools from network analysis, such as those based on exploration of mesoscale structures, also promise to yield fascinating insights into investigations of physical networks. In particular, examining how network analysis can contribute to forecasting not only where, but also when, failures occur in disordered networks is a central point for future studies.

In our investigation, we found that calculations based on shortest paths can help forecast failure locations in disordered lattices. Specifically, calculating the geodesic betweennesses of the edges in a network permits one to assess which edges are more prone to failure than others. Considering only edges with values above the mean GEBC of a network allows one to discard a large fraction of edges as unlikely failure locations. This feature of our test makes it very valuable, especially because it avoids a detailed analysis of energetics.

Combined with refs. 37 and 38, our work provides evidence that betweenness centrality successfully identifies physical properties in both granular packings and lattices that are derived from them. Similarly, analyses inspired by rigidity percolation

in granular materials have identified that our disordered lattices undergo a ductile–brittle failure transition as a function of connectivity \bar{z}_0 , as determined by counting degrees of freedom and constraints (23). We have focused on testing the sensitivity and specificity of our approach in the context of disordered lattices that we generated from force networks in quasi-2D granular packings, and this does not ensure its success for other network structures. Indeed, it has been established that the origin of a disordered structure—whether from numerical spring networks, frictionless jammed sphere packings, or pruned networks—can strongly affect elastic responses and the rigidity transition (52, 53). Therefore, we expect that both the granular origins of our samples (and hence their geometry) may affect the particular failure behavior that we have observed in this study. Collectively, these investigations (and our investigations) point toward a need to understand the importance of network topology and geometry themselves, regardless of their manifestation as a granular packing or a lattice. This is an important step toward distinguishing between geometric effects and system-specific physical effects. Therefore, an important future direction is to examine networks that one obtains by other methods. Examples include overconstrained granular packings, leaf-venation patterns, and randomly pruned crystalline lattices.

Our work also opens the door for structure design and the purposeful setting of desired failure locations. One can build particular network topologies into designed materials that permit the constraining of failures to regions of a sample or, by contrast, promote desirable patterns of damage spreading to ensure the robustness of structures.

Materials and Methods

Experimental Samples. We conduct experiments on a set of disordered structures that we derived from experimentally determined force networks in granular materials, as done in Berthier et al. (23). The original data used in the paper is available in the Dryad repository (22). The methodology to create these experimental samples is inspired by refs. 4, 9, 10, 52, and 53, which performed similar processes numerically. We begin from observed force-chain structures in a quasi-2D photoelastic granular material. The granular packings consist of $N = 824$ bidisperse circular discs (of 2 distinct radii, r_1 and r_2 , with $r_1/r_2 = 1.4$) in approximately equal numbers (Fig. 1A). We uniaxially load each packing under a series of finite displacements of one wall, generating multiple realizations of both packings and force networks.

Using an open-source photoelastic solver that is based on the method described in ref. 21, we identify all load-bearing contacts in a system, yielding a network of physical connections between particles that we use to generate a disordered lattice (Fig. 1B). We construct a network by assigning each particle center as a node of a graph G and then placing an edge between 2 nodes wherever we observe a load-bearing contact. The network is associated with an $N \times N$ binary (i.e., unweighted) adjacency matrix A , with elements

$$A_{ij} = \begin{cases} 1, & \text{if particles } i \text{ and } j \text{ are load bearing,} \\ 0, & \text{otherwise.} \end{cases} \quad [3]$$

We showed an example network in Fig. 1C. It is undirected, because each contact is bidirectional; its associated adjacency matrix is therefore symmetric about the diagonal ($A_{ij} = A_{ji}$).

We laser cut the physical samples from acrylic plastic sheets (with an elastic modulus of about 3 GPa) of thickness $h = 3.17$ mm. Each edge becomes a beam of width 1.5 mm; beams intersect at cross-links that correspond to the centers of particles (i.e., the nodes), and the particles' radii set the length of the beams. We adopt the term “cross-link” from the study of fiber networks (2, 18), which consist of filaments (bonds) that are bound via cross-linkers that either allow energy-free rotations or associate angular variations to a finite cost of energy (as “welded” cross-links). We showed an example sample in Fig. 1D; note that samples that we construct multiple times based on the same mathematical networks by cutting from different sheets of material are not perfectly identical due to small details of processing during cutting.

A simple characteristic of a network is its mean degree \bar{z} (also known as the “connectivity” or “coordination number”), which is equal to the mean number of edges per node. That is,

$$\bar{z} = \frac{1}{2N} \sum_{ij} A_{ij}. \quad [4]$$

It is known that the bulk properties of amorphous solids (23, 54) are influenced strongly by \bar{z} . We use the subscript 0 to denote initial networks (i.e., networks before any subsequent modifications from lattice beam failures). We study 6 different initial networks, with mean degrees $\bar{z}_0 = \{2.40, 2.55, 2.60, 3.00, 3.35, 3.60\} \pm 0.02$, which we draw from 2 different initial granular configurations. We do a total of 14 experiments; we test each network at least once in compression and once in tension. For the networks with $\bar{z}_0 = 2.60$ and $\bar{z}_0 = 3.00$, we do an additional tensile test on a second set of fully intact samples. To obtain a sample that is as close as possible to the isostatic value $\bar{z}_{iso} = 3.00$ of an infinite-friction packing (55), we prune a network that initially has a value of $\bar{z}_0 = 3.60$ by progressively removing its contacts with the smallest force values.

Mechanical Testing Protocol. We perform compression and tension tests using an Instron 5940 Single Column system with a 2-kN load cell. We use a displacement rate of 1.0 mm/min for tension experiments and 1.5 mm/min for compression experiments. In compression, we confine a sample between 2 parallel acrylic plates to constrain out-of-plane buckling. We record each experiment using a Nikon D850 digital camera at a frame rate of 24 or 60 fps. During the course of each experiment, beams break throughout a sample as damage progresses. Using the time series of measured compressive and tensile forces, we identify each failure event, which corresponds to a set of 1 or more breakages that occur simultaneously. Our frame rates are insufficient to distinguish multiple successive breakage events that occur within a single failure event, but they are sufficient to easily separate the failure events from each other. In all cases, we are able to determine the locations of individual beam failures by examining the images collected immediately after a recorded drop in force. The failure events occur sequentially, deteriorating the structure until complete failure of a sample. This corresponds to a crack spanning the sample from one lateral side to the other, such that there is no set of beams that connects the top and bottom boundaries.

As damage progresses, the adjacency matrix A (and the associated network G) (Eq. 3) that encodes the network structure changes after each failure event. When the beam that connects nodes i and j fails, we set $A_{ij} = A_{ji} = 0$ to record this event. We thus do a series of computations on networks that are based on measurements at a particular strain step s , which is associated with an applied strain value ε . We distinguish between the initial network G_0 (with adjacency matrix A_0), which is associated with a fully intact sample, and altered networks G_s (with associated adjacency matrices A_s).

Note that, as characterized in ref. 23, both tensile and compressive loading of samples with $\bar{z}_0 < \bar{z}_{iso}$ will fail from breakages that are well-separated in time and are spatially spread out in a sample (i.e., ductile-like failure). By contrast, it was shown in ref. 23 that, for $\bar{z}_0 > \bar{z}_{iso}$, a few temporally separated breakages take place before the samples break abruptly and all of the failed beams are localized, forming a narrow crack (i.e., brittle-like failure). Therefore, for the samples with $\bar{z}_0 = 3.35$ and $\bar{z}_0 = 3.60$, the deterioration of a sample's structure occurs via both small (1 to 3 breakages at a time) and large (more than 3 simultaneous breakages) failure events. In our analysis, we remove corresponding edges from the networks as failures take place, and we then perform fresh calculations of centrality. Our analysis of failure locations excludes the large events, because we are specifically interested in the progression of failures. Our results are qualitatively similar for samples tested in tension vs. in compression. Therefore, we do not distinguish between these 2 loading conditions in our analysis.

GEBc. Because failures in our samples consist mostly of breaking beams (rather than the thicker cross-links), we focus on an edge-based counterpart of geodesic node betweenness centrality (25). This measure gives insight into the importance of edges in a network in terms of how often they are on shortest paths between origin and destination nodes. Considering an edge e_{ij} that links nodes i and j in a graph G , we calculate a symmetric GEBc matrix based on the fraction of shortest paths that traverse an edge when considering all origin–destination pairs of nodes in a network (including nodes i and j) (31):

$$E_{ij} = \sum_{s \neq t} \frac{\sigma_{st}(e_{ij})}{\sigma_{st}}, \quad [5]$$

where σ_{st} is the number of shortest paths from node s to node t and $\sigma_{st}(e_{ij})$ is the number of those paths that include the edge e_{ij} . We compute E_{ij} using open-source code from ref. 51 (which uses an algorithm that is a slight modification of the one in ref. 56). Computing GEBcs can be computationally costly for large networks. The computation time to calculate GEBc for all

edges is $\mathcal{O}(Nm)$ for sparse networks, where N and m denote the numbers of nodes and edges, respectively, of a network (25). All of our graphs G are undirected and unweighted, but one can also study notions of edge betweenness centrality for directed and weighted graphs.

It is common to normalize E_{ij} by $\frac{1}{2}N(N-1) - 1$ (i.e., the number of edges other than the one under consideration) (57) or by $(N-1)(N-2)/2$ (i.e., the number of node pairs) (31) to ensure that GEBC values lie between 0 and 1. However, because we compare the relative importance of edges to others in a given network and as successive edge removals occur, we use a different normalization. In our calculations, for a given network at strain step s and characterized by its adjacency matrix A_s (where $s=0$ for the initial network), we define the normalized GEBC matrix $\bar{E}_s = E_s/\bar{E}_s$, where \bar{E}_s is the mean over all edges of the network G_s . To study the importance of the failing beams, for each strain step, we compute the matrix \bar{E}_s and extract the values \bar{E}_f of the edges that fail in the next failure event.

RFN Model. We create an RFN (17, 39) in which each fuse matches an edge of the network for one of our samples. All fuses have identical conductance,

1. L. J. Gibson, M. F. Ashby, G. S. Schajer, C. I. Robertson, The mechanics of two-dimensional cellular materials. *Proc. R. Soc. A* **382**, 25–42 (1982).
2. C. Broedersz, F. MacKintosh, Modeling semiflexible polymer networks. *Rev. Mod. Phys.* **86**, 995–1036 (2014).
3. K. Bertoldi, V. Vitelli, J. Christensen, M. van Hecke, Flexible mechanical metamaterials. *Nat. Rev. Mater.* **2**, 17066 (2017).
4. C. P. Goodrich, A. J. Liu, S. R. Nagel, The principle of independent bond-level response: Tuning by pruning to exploit disorder for global behavior. *Phys. Rev. Lett.* **114**, 225501 (2015).
5. J. W. Rocks et al., Designing allostery-inspired response in mechanical networks. *Proc. Natl. Acad. Sci. U.S.A.* **114**, 2520–2525 (2017).
6. P. A. Janmey, J. P. Winer, J. W. Weisel, Fibrin gels and their clinical and bioengineering applications. *J. R. Soc. Interf.* **6**, 1–10 (2009).
7. J. Knippers, K. G. Nickel, T. Speck, *Biomimetic Research for Architecture and Building Construction, Biologically-Inspired Systems* (Springer International Publishing, Cham, Switzerland, 2016).
8. M. Hanifpour, C. F. Petersen, M. J. Alava, S. Zapperi, Mechanics of disordered auxetic metamaterials. *Eur. Phys. J. B* **91**, 271 (2018).
9. D. R. Reid et al., Auxetic metamaterials from disordered networks. *Proc. Natl. Acad. Sci. U.S.A.* **115**, E1384–E1390 (2018).
10. M. M. Driscoll et al., The role of rigidity in controlling material failure. *Proc. Natl. Acad. Sci. U.S.A.* **113**, 10813–10817 (2016).
11. L. Zhang, X. Mao, Fracturing of topological Maxwell lattices. *New J. Phys.* **20**, 063034 (2018).
12. A. A. Griffith, VI. The phenomena of rupture and flow in solids. *Phil. Trans. R. Soc. Lond. A* **221**, 163–198 (1921).
13. S. Roux, A. Hansen, H. Herrmann, E. Guyon, Rupture of heterogeneous media in the limit of infinite disorder. *J. Stat. Phys.* **52**, 237–244 (1988).
14. M. J. Alava, P. K. V. V. Nukala, S. Zapperi, Role of disorder in the size scaling of material strength. *Phys. Rev. Lett.* **100**, 055502 (2008).
15. A. Shekhawat, S. Zapperi, J. P. Sethna, From damage percolation to crack nucleation through finite size criticality. *Phys. Rev. Lett.* **110**, 185505 (2013).
16. W. A. Curtin, H. Scher, Brittle fracture in disordered materials: A spring network model. *J. Mater. Res.* **5**, 535–553 (1990).
17. B. Kahng, G. G. Batrouni, S. Redner, L. de Arcangelis, H. J. Herrmann, Electrical breakdown in a fuse network with random, continuously distributed breaking strengths. *Phys. Rev. B* **37**, 7625–7637 (1988).
18. L. Zhang, D. Z. Rocklin, L. M. Sander, X. Mao, Fiber networks below the isotropic point: Fracture without stress concentration. *Phys. Rev. Mater.* **1**, 052602(R) (2017).
19. X. Mao, T. C. Lubensky, Maxwell lattices and topological mechanics. *Ann. Rev. Condens. Matter Phys.* **9**, 413–433 (2018).
20. A. Tordesillas, S. Kahagalage, C. Ras, M. Nitka, J. Teichman, Interdependent evolution of robustness, force transmission and damage in a heterogeneous quasi-brittle granular material: From suppressed to cascading failure. arXiv:1809.01491 (30 August 2018).
21. K. E. Daniels, J. E. Kollmer, J. G. Puckett, Photoelastic force measurements in granular materials. *Rev. Sci. Instrum.* **88**, 051808 (2017).
22. Berthier E et al., Data from “Rigidity percolation control of the brittle-ductile transition in disordered networks.” Dryad Digital Repository. <https://doi.org/10.5061/dryad.q1g5279>. Accessed 17 July 2019.
23. E. Berthier et al., Rigidity percolation control of the brittle-ductile transition in disordered networks. *Phys. Rev. Mater.* **3**, 075602 (2019).
24. L. Papadopoulos, M. A. Porter, K. E. Daniels, D. S. Bassett, Network analysis of particles and grains. *J. Complex Networks* **6**, 485–565 (2018).
25. M. Girvan, M. E. J. Newman, Community structure in social and biological networks. *Proc. Natl. Acad. Sci. U.S.A.* **99**, 7821–7826 (2002).
26. P. Crucitti, V. Latora, S. Porta, Centrality measures in spatial networks of urban streets. *Phys. Rev. E* **73**, 036125 (2006).
27. S. H. Lee, M. Cucuringu, M. A. Porter, Density-based and transport-based core-periphery structures in networks. *Phys. Rev. E* **89**, 032810 (2014).
28. E. Katifori, M. O. Magnasco, Quantifying loopy network architectures. *PLoS One* **7**, e37994 (2012).
29. S. H. Lee, M. D. Fricker, M. A. Porter, Mesoscale analyses of fungal networks as an approach for understanding phenotypic traits. *J. Complex Networks* **5**, 145–159 (2017).
30. M. Barthelemy, Spatial networks. *Phys. Rep.* **499**, 1–101 (2011).
31. M. Barthelemy, *Morphogenesis of Spatial Networks* (Lecture Notes in Morphogenesis, Springer International Publishing, Cham, Switzerland, 2018).
32. M. E. J. Newman, *Networks* (Oxford Univ Press, Oxford, UK, ed. 2, 2018).
33. A. Smart, J. M. Ottino, Granular matter and networks: Three related examples. *Soft Matter* **4**, 2125–2131 (2008).
34. D. S. Bassett, E. T. Owens, K. E. Daniels, M. A. Porter, Influence of network topology on sound propagation in granular materials. *Phys. Rev. E* **86**, 041306 (2012).
35. S. Wasserman, K. Faust, *Social Network Analysis: Methods and Applications* (Cambridge Univ Press, Cambridge, UK, 1994).
36. L. C. Freeman, A set of measures of centrality based on betweenness. *Sociometry* **40**, 35–41 (1977).
37. J. E. Kollmer, K. E. Daniels, Betweenness centrality as predictor for forces in granular packings. *Soft Matter* **15**, 1793–1798 (2019).
38. A. Smart, P. Umbanhowar, J. Ottino, Effects of self-organization on transport in granular matter: A network-based approach. *Europhys. Lett.* **79**, 24002 (2007).
39. L. de Arcangelis, S. Redner, H. Herrmann, A random fuse model for breaking processes. *J. Phys. Lett.* **46**, 585–590 (1985).
40. M. J. Alava, P. K. V. V. Nukala, S. Zapperi, Statistical models of fracture. *Adv. Phys.* **55**, 349–476 (2006).
41. S. Zapperi, A. Vespignani, H. E. Stanley, Plasticity and avalanche behaviour in microfracturing phenomena. *Nature* **388**, 658–660 (1997).
42. R. C. Hidalgo, Y. Moreno, F. Kun, H. J. Herrmann, Fracture model with variable range of interaction. *Phys. Rev. E* **65**, 046148 (2002).
43. E. Berthier, V. Démery, L. Ponsion, Damage spreading in quasi-brittle disordered solids. I. Localization and failure. *J. Mech. Phys. Sol.* **102**:101–124 (2017).
44. B. Lion, M. Barthelemy, Central loops in random planar graphs. *Phys. Rev. E* **95**, 042310 (2017).
45. T. S. Majmudar, R. P. Behringer, Contact force measurements and stress-induced anisotropy in granular materials. *Nature* **435**, 1079–1082 (2005).
46. E. S. Billig, J. E. Kollmer, K. E. Daniels, Protocol dependence and state variables in the force-moment ensemble. *Phys. Rev. Lett.* **122**, 038001 (2019).
47. A. M. Šimundić, Measures of diagnostic accuracy: Basic definitions. *Electron. J. Int. Fed Clin Chem. Lab Med.* **19**, 203–211 (2009).
48. M. H. Zweig, G. Campbell, Receiver-operating characteristic (ROC) plots: A fundamental evaluation tool in clinical medicine. *Clin. Chem.* **39**, 561–577 (1993).
49. M. Barthelemy, Betweenness centrality in large complex networks. *Eur. Phys. J. B* **38**, 163–168 (2004).
50. S. Scellato, A. Cardillo, V. Latora, S. Porta, The backbone of a city. *Eur. Phys. J. B* **50**, 221–225 (2006).
51. Brain connectivity toolbox. <https://sites.google.com/site/bctnet/>. Accessed 30 August 2018.
52. W. G. Ellenbroek, Z. Zeravcic, W. van Saarloos, M. van Hecke, Non-affine response: Jammed packings vs. spring networks. *Europhys. Lett.* **87**, 34004 (2009).
53. W. G. Ellenbroek, V. F. Hagh, A. Kumar, M. F. Thorpe, M. van Hecke, Rigidity loss in disordered systems: Three scenarios. *Phys. Rev. Lett.* **114**, 135501 (2015).
54. M. Wyart, On the rigidity of amorphous solids. *Ann. Phys. Fr.* **30**, 1–96 (2005).
55. S. Henkes, D. A. Quint, Y. Fily, J. Schwarz, Rigid cluster decomposition reveals criticality in frictional jamming. *Phys. Rev. Lett.* **116**, 028301 (2016).
56. U. Brandes, A faster algorithm for betweenness centrality. *J. Math. Sociol.* **25**, 163–177 (2001).
57. G. Chen, X. Wang, X. Li, “Preliminaries” in *Fundamentals of Complex Networks* (Wiley–Blackwell, Hoboken, NJ, 2015), pp. 15–101.

1

2 **Supplementary Information for**

3 **Forecasting failure locations in two-dimensional disordered lattices**

4 **Estelle Berthier, Mason A. Porter, and Karen E. Daniels**

5 **Estelle Berthier.**

6 **E-mail: ehberthi@ncsu.edu**

7 **This PDF file includes:**

8 Supplementary text

9 Figs. S1 to S5

10 Supporting Information Text

11 **Random-fuse network (RFN) current versus geodesic edge betweenness (GEBC) tests of failure locations.** To elucidate the
12 role of geometry in capturing failure locations, we compare the forecasting ability of a test that uses current that we compute
13 from a random-fuse network (RFN) model to that of a test that uses geodesic edge betweenness centrality (GEBC). In the
14 left axis of Fig. S1A left, we show the fraction of edges in a network with a current \tilde{I} (respectively, GEBC \tilde{E}) that is larger
15 than a threshold current \tilde{I}_{th} (respectively, threshold GEBC \tilde{E}_{th}). On the right axis, we show the failure rate as the fraction
16 of misdiagnosed edges, which we define as failed edges with a current (respectively, GEBC) that is less than or equal to the
17 threshold current (respectively, threshold GEBC). That is, $\tilde{I}_f \leq \tilde{I}_{\text{th}}$ (respectively, $\tilde{E}_f \leq \tilde{E}_{\text{th}}$) as a function of the threshold.

18 To explain the small improvement that we obtain when using a model with physical considerations (the RFN-based test),
19 we show in Fig. S1B the relation between the current (\tilde{I}_f) of failed edges and the GEBC (\tilde{E}_f) of these edges. The Pearson
20 correlation coefficient between these two quantities is $R \approx 0.81$.

21 These two tests are not systematically misdiagnosing (obtaining a false negative outcome) failure locations for the same
22 edges. We show this in Fig. S2, where we plot the fraction of failed edges that are misdiagnosed using the RFN-based test and
23 correctly diagnosed using the GEBC-based test as a function of the threshold. (Depending on the test, this is either a current
24 threshold or a GEBC threshold.)

25 **Dependency of current on orientation.** Consider a special case of a perfectly ordered squared lattice with identical resistors
26 on each edge and a voltage difference that we apply across the top and bottom boundaries. In this configuration, no current
27 flows in the horizontal edges. (This contrasts with the situation for GEBC, which is orientation-independent.) Therefore, we
28 expect that — to an extent that depends on the amount of structural disorder — any anisotropy remains imprinted in the
29 current flow in the system. Indeed, as we see in Fig. S3A, there is a strong dependence of the edge voltage on the edge angle
30 (between 0 and 90 degrees) with respect to the vertical loading for a network with connectivity (i.e., mean degree) $\bar{z}_0 = 3.60$.
31 The Spearman rank-correlation coefficient is $\rho \approx 0.77$.

32 To determine the effect of this dependency on the forecasting ability of the RFN-based test, we show in Fig. S3B, for various
33 current thresholds \tilde{I}_{th} , the fraction P of misdiagnosed edges (\tilde{I}_f^-) that have an orientation with an angle θ that is smaller than
34 a threshold θ_{th} . We thereby identify a bias towards misdiagnosing edges that are almost perpendicular (i.e., those with small θ)
35 to the loading vertical direction.

36 **Dependency of GEBC on edge distance to the boundaries.** Because one computes the GEBC of an edge based on the fraction
37 of shortest paths that traverse an edge when considering all origin–destination pairs of nodes in a network, we expect edges near
38 boundaries to have smaller values of \tilde{E} , and we hence expect that they will be misdiagnosed more frequently by a GEBC-based
39 test than edges that are located near the center of a network. To assess this possible limitation of our GEBC-based test, we
40 calculate (in terms of the number of edges) the normalized shortest-path distance δ to reach a node on a boundary starting
41 from a given node in the network. The normalized shortest-path distance ranges from 0 (for a node on a boundary) to 1 (if
42 its shortest-path length to a boundary is the longest in a network). Therefore, nodes near boundaries have values of δ that
43 are close to 0, and those that are near the center of a network have values that are close to 1. Specifically, the normalized
44 shortest-path distance for a node i in a network G is

$$45 \delta_i = 1 - \min_{j \in \mathcal{B}} \left(\frac{d^{\max} - d_{ij}}{d^{\max}} \right), \quad [1]$$

46 where \mathcal{B} is the set of boundary nodes and d^{\max} is the distance of a longest path between a node and a boundary in the network.
47 We define the boundary \mathcal{B} as the set of nodes that are located within one radius (where the radius is equal to half of the length
48 of the longest beam in the network) from the nodes with highest or lowest vertical position (i.e., top or bottom nodes) and
49 highest or lowest horizontal position (i.e., leftmost or rightmost nodes).

50 For each failing edge, we compute the normalized shortest-path distance for both nodes that are associated with the edge,
51 and we take the smaller value to define δ_f for each such edge. In Fig. S4A, we show the histogram of distances δ_f ; and we
52 thereby highlight that failing edges occur at all (normalized shortest-path) distances from the boundaries. However, as we show
53 in Fig. S4B, most misdiagnosed edges tend to occur near boundaries.

54 **A comparison between the RFN model and GEBC on a small network.** In Fig. S5, we show a schematic that highlights the
55 fundamental difference between the RFN model and GEBC. Specifically, the latter is independent of the loading direction,
56 whereas the former depends on it. In the simple example in this schematic, when we load the top and bottom nodes (see
57 the arrows), we observe that the stresses in each beam change if we rotate the configuration by 90 degrees. This is captured
58 successfully by the RFN, which identifies the fact that different current values flow in each edge. Note, however, that the RFN
59 model does not systematically predict the correct stress distribution: the central horizontal edge (in the top configuration) has
60 a null current, whereas this beam is stressed if we load the corresponding beam structure. By contrast, the GEBC values
61 do not change when we rotate the structure. Therefore, GEBC is unable to capture physical properties at the scale of a few
62 edges. Nevertheless, as these effects effectively average over multiple directions in our disordered lattices, GEBC and the RFN
63 measure similar values on average, and the GEBC-based test performs well at the scale of our samples.

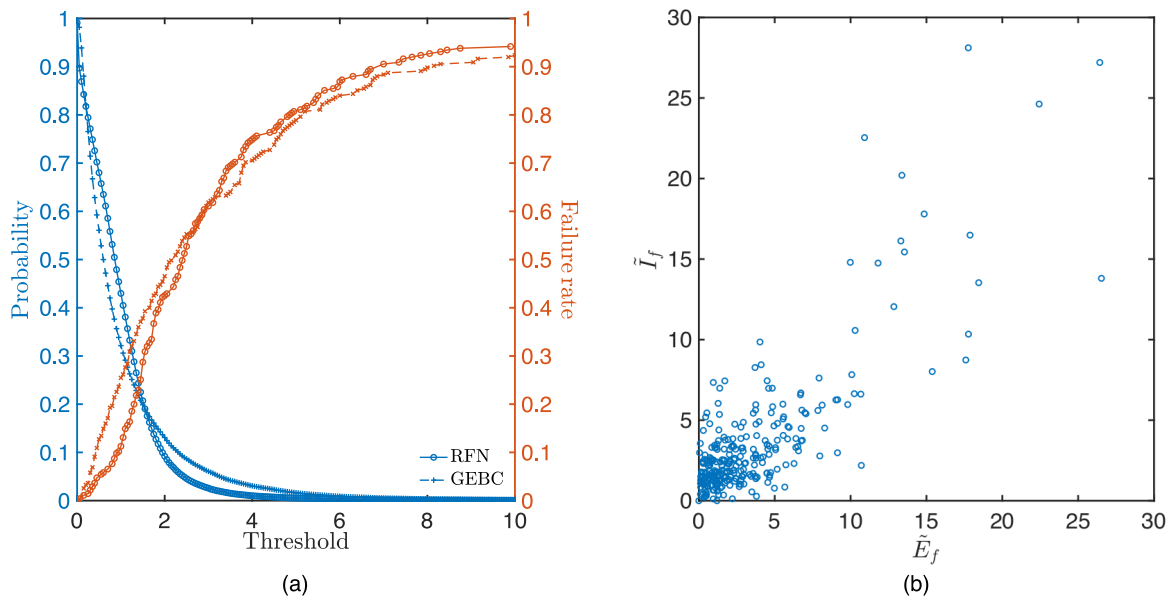


Fig. S1. (a) Comparison of the ability of the tests to forecast failure locations using currents from a random-fuse network (RFN; curves with circles) and geodesic edge betweenness centrality (GEBC; curves with crosses). On the left axis (in blue), we show the fraction of edges in a network for which the current is above a certain threshold (i.e., $\tilde{I} > \tilde{I}_{th}$) and the fraction of edges for which GEBC is above a certain threshold (i.e., $\tilde{E} > \tilde{E}_{th}$). On the right axis (in orange), we show the fraction of failed beams for which $\tilde{I} \leq \tilde{I}_{th}$ and $\tilde{E} \leq \tilde{E}_{th}$. The axis label “Threshold” indicates \tilde{I}_{th} for the RFN-based test and \tilde{E}_{th} for the GEBC-based test. (b) Scatter plot between the current (\tilde{I}_f) and GEBC (\tilde{E}_f) of failed edges. The Pearson correlation coefficient between \tilde{I}_f and \tilde{E}_f is $R \approx 0.81$.

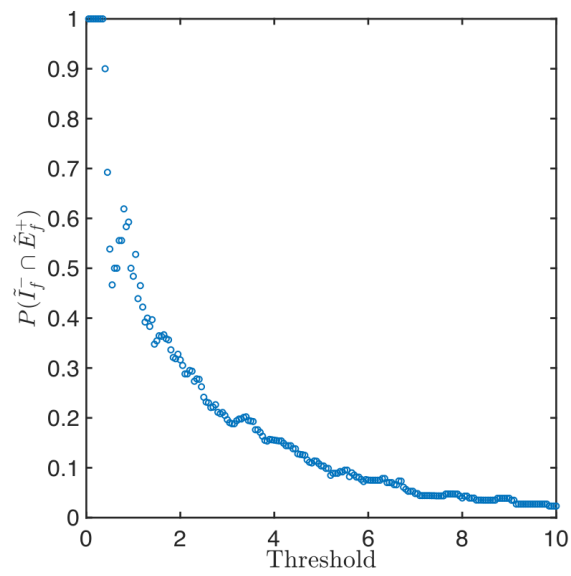


Fig. S2. Probability $P(\tilde{I}_f^- \cap \tilde{E}_f^+)$ that a misdiagnosed edge from the RFN-based test is diagnosed successfully using the GEBC-based test. The quantity \tilde{I}_f^- denotes an edge that is misdiagnosed using the RFN-based test (i.e., $\tilde{I}_f \leq \tilde{I}_{\text{th}}$), the quantity \tilde{E}_f^+ denotes an edge that is diagnosed successfully using the GEBC-based test (i.e., $\tilde{E}_f > \tilde{E}_{\text{th}}$), and $\tilde{I}_f^- \cap \tilde{E}_f^+$ denotes an edge that is misdiagnosed using the RFN-based test but diagnosed correctly using the GEBC-based test. The axis label “Threshold” indicates the current \tilde{I}_{th} for the RFN-based test and the GEBC \tilde{E}_{th} for the GEBC-based test.

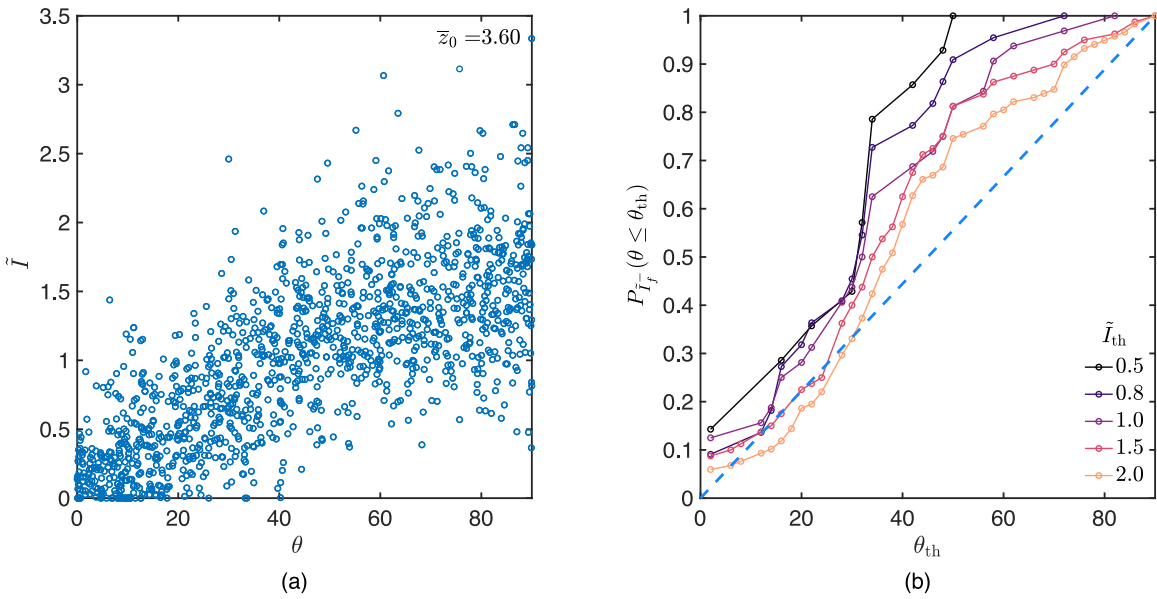


Fig. S3. (a) For the initial network with connectivity $\bar{z}_0 = 3.60$, we show a scatter plot between edge current \tilde{I} and the edge orientation θ between 0 degrees and 90 degrees. (b) For different values of the current threshold, we show the probability $P_{\tilde{I}_f^-}$ that a misdiagnosed failed edge (i.e., with a current of $\tilde{I}_f \leq \tilde{I}_{th}$), which is denoted by \tilde{I}_f^- , has an orientation θ that is less than or equal to a threshold value θ_{th} . The dashed blue line indicates the theoretical behavior of misdiagnosed edges with no preferred orientation.

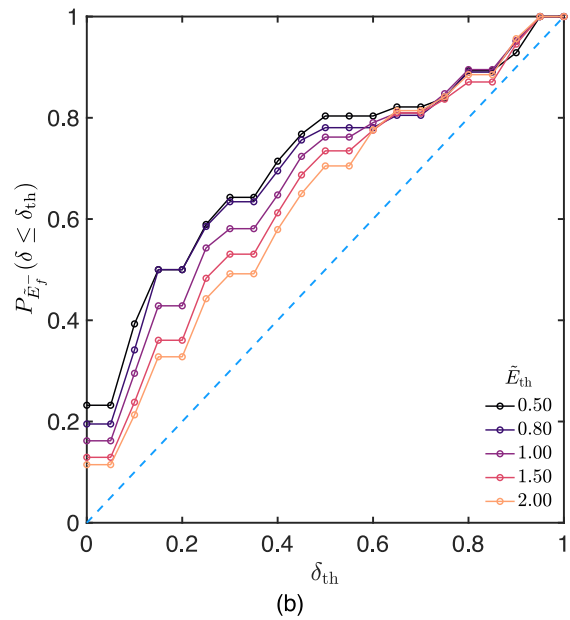
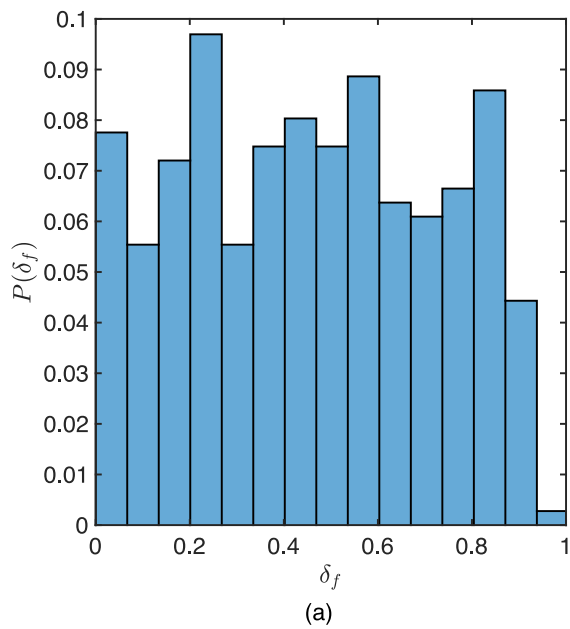


Fig. S4. (a) Histogram of δ_f , the normalized shortest-path distance of failing edges to a boundary. (See the definition in the main text.) (b) For different GEBC threshold values \tilde{E}_{th} , we show the probability that a misdiagnosed failed edge (i.e., ones with with a GEBC of $\tilde{E}_f \leq \tilde{E}_{th}$), which we denote by \tilde{E}_f^- , is located at a distance δ_f that is less than or equal to a threshold value δ_{th} . The dashed blue line indicates the theoretical behavior of misdiagnosed edges with no preferred (normalized shortest-path) distance to the boundary in a network.

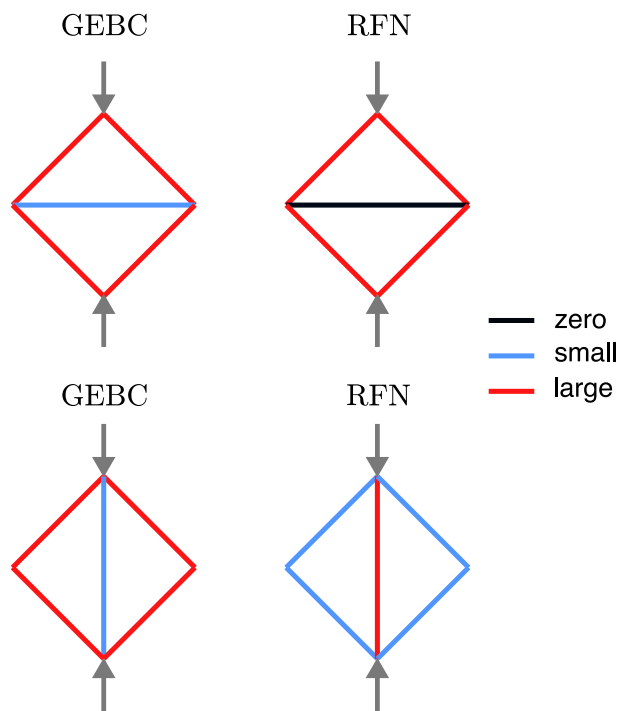


Fig. S5. Random-fused network versus geodesic edge betweenness centrality at the scale of few edges. When we load the top and bottom nodes, the GEBC distribution is the same in the top and bottom configurations; by contrast, the RFN current distribution is different in these two configurations.